Preprint

Enrichment of the dust-to-gas mass ratio in Bondi/Jeans accretion/cloud systems due to unequal changes in dust and gas incoming velocities

P. M. Bellan

Applied Physics, Caltech, Pasadena CA 91125, USA

pbellan@caltech.edu

ABSTRACT

The ratio of the Bondi and Jeans lengths is used to develop a cloud-accretion model that describes both an inner Bondi-type regime where gas pressure is balanced by the gravity of a central star and an outer Jeans-type regime where gas pressure is balanced by gas self-gravity. The gas density profile provided by this model makes a smooth transition from a wind-type inner solution to a Bonnor-Ebert type outer solution. It is shown that high-velocity dust impinging on this cloud will tend to pile-up due to having a different velocity profile than gas so that the dust-to-gas ratio is substantially enriched above the 1% ISM level.

1. Introduction

Laboratory-scale plasma jets have been produced by a magnetohydrodynamic mechanism believed analogous to the mechanism responsible for driving astrophysical jets (Hsu & Bellan 2002; Bellan *et al.* 2005). The laboratory jets are driven by capacitor bank power supplies that provide poloidal and toroidal magnetic fields and the jet acceleration mechanism can be considered as due to the pressure of the toroidal magnetic field inflating flux surfaces associated with the poloidal magnetic field. If these jets are indeed related to astrophysical jets, the obvious question arises as to what constitutes the power supply responsible for the toroidal and poloidal magnetic fields in the astrophysical situation. Existing models of astrophysical jets typically assume the poloidal field is simply given and that the toroidal field results from the rotation of an accretion disk twisting up the assumed poloidal field. The

author has developed an alternate model which postulates that the toroidal and poloidal field result instead from a dusty plasma dynamo mechanism that converts the gravitational energy of infalling dust grains into an electrical power source that drives poloidal and toroidal electric currents creating the respective toroidal and poloidal fields. A brief outline of how infalling charged dust can drive poloidal currents has been presented in Bellan (2007).

An important requirement of the model is that there should be sufficient infalling dust to provide the jet power. It has been well established that the dust-to-gas mass ratio in the Interstellar Medium (ISM) is 1%. If one assumes, as has been traditional, that this ratio holds throughout the accretion process, then the gravitational energy available from infalling dust would be insufficient. However, Fukue (2001) has recently shown via numerical solution of coupled dust and gas equations of motion that the dust-to-gas ratio can become substantially enriched during Bondi-type accretion.

Star formation has also been previously examined from a molecular cloud physics point of view which differs significantly from the Bondi accretion point of view in the treatment of self-gravity and inflows. Molecular cloud physics is clearly important because observations indicate that stars form within the dense cores of molecular clouds (e.g., see Evans *et al.* (2001)). Analysis of the force balance in molecular clouds shows that the cloud radial density profile can be characterized by the Bonnor-Ebert sphere solution (Ebert 1955; Bonnor 1956). This solution does not take into account flows associated with accretion. Dust dynamics is also not taken into account; instead it is typically assumed that the dust-to-gas mass ratio is fixed at 1% for all radii.

To summarize the above discussion, we note that the Bondi-type analysis reported by Fukue (2001) emphasizes inflow physics and dust-gas coupling but does not take into account self-gravity whereas molecular cloud analysis such as used by Evans *et al.* (2001) emphasizes self-gravity, but does not take into account inflow or dust-gas coupling.

This paper will address the physics of coupled dust and gas accretion using a methodology similar in concept to that presented by Fukue (2001), but extended to bridge the gap between Bondi accretion models and molecular cloud force balance models. The enrichment mechanism observed by Fukue (2001) will be examined in detail and will be shown to result from the inherently non-uniform nature of the Bondi/molecular cloud/ISM system. Properties of dust and gas for radii ranging from the cloud-ISM interface to the inner Bondi region will be considered by examining a sequence of successively smaller concentric regions. The basic character of each region and its scale, defined in terms of the nominal radial distance from a central object star, is as follows:

ISM scale: The outermost scale is that of the Interstellar Medium (ISM). The ISM has

a gas density $\sim 10^7$ m^{-3}, a dust-to-gas mass ratio of 1 percent, a gas temperature $T_g^{ISM} \sim 100$ K, and is optically thin. The ISM is assumed to be spatially uniform and to bound a molecular cloud having radius r_{edge}.

Molecular cloud scale: The molecular cloud scale has much higher density than the ISM and is characterized by force balance between gas self-gravity and gas pressure. The molecular cloud scale is sub-divided into a large, radially non-uniform low-density outer region and a small, approximately uniform, high-density inner core region. Clouds have a characteristic scale given by the Jeans length r_J. The radial dependence of density is provided by the Bonnor-Ebert sphere solution which acts as the outer boundary of the Bondi accretion scale.

Bondi accretion scale: The Bondi accretion scale (Bondi 1952) is $\sim r_B$ which is sufficiently small that gas self-gravity no longer matters so equilibrium is instead obtained by force balance between gas pressure and the gravity of a central object assumed to be a star having mass M_*. The Bondi scale is sub-divided into three concentric radial regions: an outermost region where the gas flow is subsonic, a critical transition radius at exactly r_B where the flow is sonic, and an innermost region where the gas flow is free-falling and supersonic.

Collisionless dusty plasma scale (to be considered in a future publication): Free-falling dust grains collide with each other in one of the above scales and coagulate to form large-radius grains which are collisionless and optically thin. The optically thin dust absorbs UV photons from the star, photo-emits electrons and becomes electrically charged. The charged dust grains are subject to electromagnetic forces in addition to gravity. Motions of charged dust grains relative to electrons result in electric currents with associated poloidal and toroidal magnetic fields [see preliminary discussion in Bellan (2007)].

Jet scale (to be considered in a future publication): The electric currents interact with the magnetic fields to produce magnetohydrodynamic forces which drive astrophysical jets in a manner analogous to that reported in Hsu & Bellan (2002) and Bellan *et al.* (2005).

The separation-of-scales requirement $r_J >> r_B$ implies existence of a small parameter

$$\varepsilon_{BJ} = \frac{r_B}{r_J} \tag{1}$$

quantifying the separation between the Bondi and Jeans scales. For purposes of relating the Bondi and Jeans scales to each other it is convenient to introduce a geometric-mean scale

with characteristic length given by

$$r_{gm} = \sqrt{r_B r_J} = \sqrt{\varepsilon_{BJ}} r_J \tag{2}$$

in which case

$$r_B \ll r_{gm} \ll r_J. \tag{3}$$

Gas and dust must be considered separately in each scale. We assume that gas motion influences dust motion but not vice-versa so that the dust dynamics can be ascertained after gas dynamics has been determined. This assumption is appropriate so long as dust mass and energy densities are small compared to corresponding gas densities or if the dust is decoupled from the gas. The sequence of scales is summarized in Tables 1 and 2. The numerical values of table elements with asterisks will be predicted by the model to be presented here while table elements with filled-in numbers represent prescribed physical boundary conditions. Here m_g is the gas molecular mass, n_g is the gas density, T_g is the gas temperature, $u_{g,d}$ are the radially inward gas and dust fluid velocities, and $\rho_{g,d}$ are the gas and dust mass densities. Quantities with superscripts 'ISM' are evaluated in the ISM, un-superscripted quantities refer to Bondi or molecular cloud regions.

Our methodology will be conceptually similar to Fukue (2001) but will also differ in important ways. Fukue (2001) used a wind equation scheme to model Bondi-type physics and, unlike the analysis to be presented here, assumed the Bondi accretion region was directly bounded by the ISM, i.e., no molecular cloud region with Jeans-type scaling was taken into account. In addition, Fukue assumed that (i) the gas was heated by the combined effects of adiabatic compression and friction due to dust-gas collisions, and (ii) the entire region was optically thin so that the dust was subject to radiation pressure. Because of the complexity introduced by the heating of the gas, Fukue obtained results via numerical solution of three coupled differential equations (gas momentum, dust momentum, gas heating). Our approach will differ by assuming that (i) the gas is isothermal, (ii) a molecular cloud region lies between the Bondi accretion region and the ISM, and (iii) the system is optically thick outside the inner part of the Bondi region so that dust is shielded from optical radiation until it penetrates to the inner part of the Bondi region. Furthermore, rather than using numerical solutions, we will attempt analytic solutions as much as possible, a goal made feasible by the isothermal assumption. We believe our assumptions (i)-(iii) reasonably correspond to observations that gas is nearly isothermal and that stars form inside the cores of optically thick molecular clouds.

region	location	n_g	T_g	u_g
ISM	$r > r_{edge}$	10^7 m^{-3}	100 K	*
B-E sphere	$r_{gm} < r < r_{edge}$	*	10 K	*
Bondi-Jeans interface	$r_{gm} = \sqrt{r_B r_J}$	*	”	*
Bondi subsonic	$r_B < r < r_{gm}$	*	”	$< \sqrt{\kappa T_g/m_g}$
Bondi transonic	$r = r_B$	*	”	$\sqrt{\kappa T_g/m_g}$
Bondi supersonic	$r < r_B$	*	”	$> \sqrt{\kappa T_g/m_g}$

Table 1: Sequence of regions for gas, * indicates quantity to be discussed/calculated in text

region	location	ρ_d/ρ_g	u_d
ISM	$r > r_{edge}$	0.01	3 km/s (turbulent acceleration)
B-E sphere	$\sqrt{r_B r_J} < r < r_{edge}$	*	slowing down by gas
Bondi-Jeans interface	$r_{gm} = \sqrt{r_B r_J}$	*	entrained with gas
Bondi subsonic	$r_B < r < r_{gm}$	*	”
Bondi transonic	$r = r_B$	*	”
Bondi supersonic	$r < r_B$	*	”

Table 2: Sequence of regions for dust physics, * indicates to be discussed/calculated in text

2. Gas and dust equations

The steady-state equation of motion for spherically symmetric gas is

$$\rho_g u_g \frac{du_g}{dr} = -\frac{\partial P_g}{\partial r} - \rho_g \frac{MG}{r^2} + f_{drag}. \tag{4}$$

Here u_g is the radial fluid velocity of the gas, $P_g = n_g \kappa T_g$ is the gas pressure, ρ_g is the gas mass density,

$$M = M_* + \int_{r_*}^{r} 4\pi\xi^2 \left(\rho_g(\xi) + \rho_d(\xi)\right) d\xi \tag{5}$$

is the mass inside a sphere of radius r, ρ_d is the dust mass density, M_* and r_* are the mass and radius of the central object star, and f_{drag} is the drag force on gas due to collisions with dust. Lamers & Cassinelli (1999) give the drag force to be

$$f_{drag} = -(u_g - u_d)\frac{\rho_g \rho_d}{m_d}\sigma_d \sqrt{c_g^2 + (u_d - u_g)^2}. \tag{6}$$

The dust behaves as a zero-pressure fluid, so its steady-state equation of motion is

$$\rho_d u_d \frac{du_d}{dr} = -\rho_d \frac{MG}{r^2} - f_{drag}. \tag{7}$$

In the limit that the integral in Eq.5 can be ignored, these are the same momentum equations considered by Fukue (2001).

Observations indicate that the gas temperature of clouds, cores, and accretion disks lies in the range 10-30 K indicating that the gas can be considered approximately isothermal. If the gas were adiabatic, i.e., if $P_g \sim \rho_g^{5/3}$ then the gas temperature would vary as $T_g \sim n^{2/3}$. Since there is at least a 10^3 increase in gas density from the cloud edge to the Bondi region inner free-fall region, an adiabatically compressed gas volume element would have its temperature increase at least one-hundred fold as it moved inwards. If in addition, there were heating of gas due to dust frictional drag, the gas temperature would increase even more. For example, the sound speed in Fukue's Fig. 1 increases by a factor of approximately 40 from right to left corresponding to a factor of 1600 increase in temperature. Thus Fukue's Fig. 1 analysis predicts that the gas temperature increases from 100 K to 1.6×10^5 K a temperature at which the molecular hydrogen would not only have become disassociated but would have turned into plasma. Since the observed gas temperature is not 1.6×10^5 K but in fact is clamped at 10-30 K, any heat energy resulting from adiabatic compression or friction must be immediately lost, presumably via molecular line emission. In order to conform to observations we therefore assume the gas is isothermal, an approximation which has the incidental, yet fortuitous side effect of making an analytic approach to the problem feasible.

Since we are assuming that the dust is a perturbation on the gas, we first solve the gas equation ignoring the dust, and then use gas equation solutions as inputs for the dust equation. This approach is self-consistent so long as the dust is approximately decoupled from the gas or if the dust mass and energy densities are much less than the gas mass and energy densities. The approach fails in situations where the dust is coupled to the gas and attains mass or energy densities comparable to the gas. However, the point at which failure occurs is interesting and can be considered a useful prediction of the model.

We now consider gas dynamics while ignoring the dust in which case the gas equation of motion reduces to

$$\rho_g u_g \frac{du_g}{dr} = - c_g^2 \frac{d\rho_g}{\partial r} - \frac{\rho_g G}{r^2}\left(M_* + \int_{r_*}^{r} 4\pi\xi^2 \rho_g(\xi) d\xi\right) \tag{8}$$

where

$$c_g = \sqrt{\frac{\kappa T_g}{m_g}} \tag{9}$$

is the gas thermal velocity.

Equation 8 has two regimes of interest, namely

1. an inner regime where r is so small that $M_* \gg \int_{r_*}^{r} 4\pi\xi^2\rho_g(\xi)d\xi$ and
2. an outer regime where r is so large that $M_* \ll \int_{r_*}^{r} 4\pi\xi^2\rho_g(\xi)d\xi$.

The former regime leads to a Bondi accretion situation characterized by the wind equation discussed by Fukue (2001) while the latter leads to a Jeans-scale problem with Bonnor-Ebert spheres as the solution. We will examine these regimes separately and then connect them using an asymptotic technique.

Because the configuration is assumed to be steady-state, the gas and dust equations of continuity give the respective accretion rates

$$\dot{M}_g = -4\pi r^2 \rho_g u_g = const. \tag{10}$$

$$\dot{M}_d = -4\pi r^2 \rho_d u_d = const. \tag{11}$$

where u_g and u_d are negative, corresponding to radial inward motion.

3. Gas

3.1. Bondi accretion region

In this region it is convenient to normalize the velocity to c_g and lengths to the Bondi radius r_B, defined as

$$r_B = \frac{M_* G}{2c_g^2} \ . \tag{12}$$

A bar will denote normalized quantities and to avoid confusing minus signs, the normalized velocity is defined to be positive so

$$\bar{u}_g = |u_g| / c_g \tag{13}$$

$$\bar{r} = r/r_B. \tag{14}$$

Also the gas mass density is normalized to its value at r_{gm}, the geometric mean of the Bondi and Jeans scales (see Eq.2), i.e.,

$$\bar{\rho}_g = \rho_g/\rho_{gm}. \tag{15}$$

Thus ρ_{gm} is the mass density at a radius much larger than the Bondi length, but much smaller than the Jeans length (see Eq.3). The normalized form of Eq.8 in the Bondi accretion region is thus

$$\bar{u}_g \frac{d\bar{u}_g}{d\bar{r}} \ = - \ \frac{d \ln \bar{\rho}_g}{d\bar{r}} \ - \frac{2}{\bar{r}^2}. \tag{16}$$

The derivative of Eq.10 gives

$$\frac{d\ln\bar{\rho}_g}{d\bar{r}} = -\frac{1}{\bar{u}_g}\frac{d\bar{u}_g}{d\bar{r}} - \frac{2}{\bar{r}} \quad . \tag{17}$$

Combining Eqs.16 and 17 gives the isothermal wind equation (Lamers & Cassinelli 1999)

$$\left(\bar{u}_g^2 - 1\right)\ \frac{d\bar{u}_g}{d\bar{r}}\ =\ 2\bar{u}_g\left(\frac{1}{\bar{r}}\ -\frac{1}{\bar{r}^2}\right). \tag{18}$$

Equation 18 gives the condition that $\bar{u}_g = 1$ must occur when $\bar{r} = 1$ in order for $d\bar{u}_g/d\bar{r}$ to be non-singular at $\bar{r} = 1$. Equation 18 can be directly integrated to give

$$\frac{\bar{u}_g^2}{2} - \ln\bar{u}_g = 2\ln\bar{r} + \frac{2}{\bar{r}} + A \tag{19}$$

where A is a constant to be determined. The sonic condition $\bar{u}_g = 1$ at $\bar{r} = 1$ gives $A = -3/2$ so Eq.19 becomes

$$\bar{u}_g\bar{r}^2 - \exp\left(\frac{\bar{u}_g^2}{2} - \frac{2}{\bar{r}} + \frac{3}{2}\right) = 0. \tag{20}$$

Equation 20, the solution to Eq.18, is a transcendental expression relating $\bar{u}_g$ and $\bar{r}$ and having two distinct roots. One root has $\bar{u}_g$ a monotonically increasing function of $\bar{r}$ and one root has $\bar{u}_g$ a monotonically decreasing function. Both roots have $\bar{u}_g = 1$ at $\bar{r} = 1$. The root where $\bar{u}_g$ is a monotonically increasing function of $\bar{r}$ (subsonic at small $\bar{r}$, supersonic at large $\bar{r}$) is relevant to stellar winds, while the monotonically decreasing root (supersonic at small $\bar{r}$, subsonic at large $\bar{r}$) is relevant to the accretion problem discussed here and by Fukue. Since $\bar{u}_g$ is subsonic at large $\bar{r}$ and supersonic at small $\bar{r}$, Eq.19 has the following limiting forms

$$\ln\bar{u}_g\ = \ln 2 - \frac{1}{2}\ln\bar{r} \quad \text{for} \quad \bar{r} \ll 1 \tag{21}$$

$$\ln\bar{u}_g = -\ 2\ln\bar{r}\ + \frac{3}{2}\ \ \text{for} \quad \bar{r} \gg 1. \tag{22}$$

The change in the slope of $\ln\bar{u}_g$ as a function of $\ln\bar{r}$ from $-1/2$ at small $\bar{r}$ to -2 at large $\bar{r}$ is evident in Fig. 1 of Fukue.

The mass accretion rate can be determined by evaluation at $\bar{r} \gg 1$ since in this limit Eq.20 gives

$$\bar{u}_g\ =\ \ \frac{1}{\bar{r}^2}\exp\left(-\frac{2}{\bar{r}} + \frac{3}{2}\right) \quad \text{for} \quad \bar{r} \gg 1. \tag{23}$$

Using Eq.23 in Eq.10 and then evaluating at r_{gm} gives the Bondi mass accretion rate

$$\dot{M}_g =\ \pi\frac{\eta\rho_{gm}M_*^2G^2}{c_g^3} \tag{24}$$

where

$$\eta(\varepsilon_{BJ}) = \exp\left(-2\sqrt{\varepsilon_{BJ}} + \frac{3}{2}\right) \tag{25}$$

is a dimensionless quantity of order unity which occurs repeatedly in the analysis to follow. The radial dependence of the gas mass density in the Bondi regime is given by

$$\rho_g(r) = \frac{\eta \rho_{gm} M_*^2 G^2}{4r^2 \left|u_g(r)\right| c_g^3} \ . \tag{26}$$

ρ_g becomes independent of r in the large r limit of the Bondi region since in this limit Eq.23 shows that $\bar{u}_g \sim 1/\bar{r}^2$. This independence permits matching the large r limit of the Bondi region solution to the small r limit of the molecular cloud region solution (given in Sec.3.2 below) since both these solutions are independent of r.

In the small $\bar{r}$ limit, Eq. 19 gives

$$\bar{u}_g \ = \ 2/\bar{r}^{1/2} \tag{27}$$

which corresponds to the free-fall velocity. Combining this with Eqs.10 and 24 gives the mass density for $r << r_B$ to be

$$\bar{\rho}_g(\bar{r}) = \frac{\eta}{2\bar{r}^{3/2}}. \tag{28}$$

The enclosed gas mass at r_B is

$$\int_0^{r_B} 4\pi r^2 \rho_g dr \simeq 4\pi \rho_{gm} r_B^3 \int_0^1 \bar{r}^2 \bar{\rho}_g d\bar{r} = \frac{4}{3}\pi\eta\rho_{gm} r_B^3 \ . \tag{29}$$

3.2. Molecular cloud region

Again ignoring dust mass and dust drag, but now assuming $\bar{r}$ is sufficiently large that $M_* \ll \int_{r_*}^r 4\pi\xi^2 \left(\rho_g(\xi)\right) d\xi$, Eq.8 becomes

$$\frac{c_g^2}{\rho_g} \frac{d\rho_g}{dr} + \frac{G}{r^2} \int_{r_*}^r 4\pi\xi^2 \rho_g(\xi) d\xi \ = 0 \tag{30}$$

where the subsonic condition $u_g^2 << c_g^2$ has been used. Gas pressure is now balanced by self-gravity rather than by the central object gravity. Equation 30 can be recast in standard form as

$$\frac{c_g^2}{4\pi G} \frac{1}{r^2} \frac{d}{dr}\left(\frac{r^2}{\rho_g}\frac{d\rho_g}{dr}\right) + \rho_g \ = 0. \tag{31}$$

We now define a new dimensionless length suitable for Eq.31, namely

$$\tilde{r} = \frac{r}{r_J} \tag{32}$$

where

$$r_J = \frac{c_g}{\sqrt{4\pi\rho_{gm}G}} \tag{33}$$

is the Jeans length.

Equation 31 assumes the dimensionless form

$$\frac{1}{\tilde{r}^2}\frac{d}{d\tilde{r}}\left(\frac{\tilde{r}^2}{\bar{\rho}_g}\frac{d\bar{\rho}_g}{d\tilde{r}}\right) + \bar{\rho}_g = 0. \tag{34}$$

For small $\bar{r}$, we wish to have a solution which is approximately constant in order to be consistent with observations. This constant should be unity in order to connect with the outer limit of the Bondi solution since the outer limit of the Bondi solution has been constructed so as to give $\rho \to \rho_{gm}$ for $r = r_{gm}$. An approximate solution to Eq.34 that does this is $\bar{\rho}_g = 1/(1+\tilde{r}^2/6)$ but this solution fails at large $\bar{r}$. However, Equation 34 has the exact solution $\bar{\rho}_g = 2/\bar{r}^2$ which is valid at all $\bar{r}$. Thus, a solution which behaves as $\bar{\rho}_g = 1/(1+\tilde{r}^2/6)$ for small $\tilde{r}$ and as $\bar{\rho}_g = 2/\tilde{r}^2$ for large $\tilde{r}$ would do the job provided these sub-solutions smoothly merge into each other and do not introduce any spurious effects at intermediate values of $\tilde{r}$. The Padé approximation

$$\bar{\rho}_g(\bar{r}) = \frac{1}{1+\frac{\tilde{r}^2}{6}\left(1+2\left(\frac{\tilde{r}^2}{15+\tilde{r}^2}\right)^2\right)} \tag{35}$$

agrees with a direct numerical solution of Eq.34 with an error less than 20% in the range $0 < \tilde{r} < 9$, an accuracy which is more than adequate for the present analysis. The factor $\left(\tilde{r}^2/(15+\tilde{r}^2)\right)^2$ can be thought of as a 'switch' which causes $\tilde{r}^2/6$ to become $\tilde{r}^2/2$ at large $\tilde{r}^2$.

At r_{gm}, the value of $\tilde{r}$ is $\tilde{r} = r_{gm}/r_J = \sqrt{\varepsilon_{BJ}}$ and so Eq.34 matches to the Bondi solution at r_{gm} since by assumption $\varepsilon_{BJ} \ll 1$.

The combined solution spanning the range $0 < r < 9r_J$ is therefore

$$\rho_g(r) = \begin{cases} \frac{\eta M_*^2 G^2}{4r^2|u_g(r)|c_g^3}\rho_{gm} & \text{for} \quad r < r_{gm} \\ \frac{\rho_{gm}}{1+\frac{r^2}{6r_J^2}\left(1+2\left(\frac{r^2}{15r_J^2+r^2}\right)^2\right)} & \text{for} \quad r_{gm} < r < 9r_J \end{cases} \tag{36}$$

where $u_g(r)$ is given by Eq.20 and both outer and inner solutions converge to ρ_{gm} at $r = r_{gm}$. Figure 1(a) plots $n_g(r) = \rho_g(r)/m_g$ using Eq.36 with the assumptions that $\varepsilon_{BJ} = 0.3$,

$M_* = 0.4M_\odot$, $T_g = 10$ K, $T_g^{ISM} = 100$ K, and $n_g^{ISM} = 10^7\mathrm{m}^{-3}$. The values of r_B, r_{gm}, and r_J are indicated by vertical dashed lines. The solid line in Fig. 1(b) plots the corresponding gas velocity $u_g(r)$; note that $u_g = c_g$ at r_B and that the gas is subsonic to the right of r_B.

Specification of ε_{BJ} determines ρ_{gm} since substitution of Eqs.12 and 33 into Eq.1 gives

$$\rho_{gm} = \varepsilon_{BJ}^2 \frac{c_g^6}{\pi M_*^2 G^3}. \tag{37}$$

The separation-of-scales condition is consistent with the assumption $M_* \ll \int_{r_*}^{r} 4\pi\xi^2\rho_g(\xi)d\xi$ for $r \gtrsim r_J$ since $\int_{r_*}^{r_J} 4\pi\xi^2\rho_g(\xi)d\xi \simeq 4\pi\rho_{gm}r_J^3/3 = M_*/6\varepsilon_{BJ}$.

Equation 37 can be used with Eq.29 to calculate the total gas mass enclosed at r_B to be

$$\int_0^{r_B} 4\pi r^2\rho_g dr = \frac{\eta}{6}\varepsilon_{BJ}^2 M_* \tag{38}$$

which is consistent with the Bondi region assumption that $\int_0^{r_B} 4\pi r^2\rho_g dr \ll M_*$.

Equations 24 and 37 show that the gas mass accretion rate can be expressed as

$$\dot{M}_g = \frac{c_g^3}{G}\varepsilon_{BJ}^2\eta. \tag{39}$$

The gas fluid velocity at r_{gm} is

$$u_g\ (r_{gm}) = -\frac{\dot{M}_g}{4\pi r_{gm}^2\rho_{gm}} = -\varepsilon_{BJ}\eta c_g. \tag{40}$$

Bondi accretion will presumably increase M_*. Because of the existence of jets, not all accreting matter will do this. However, for purposes of estimation, if one assumes that all accreting material causes an increase in M_*, then r_B which is proportional to M_* will increase. On the other hand r_J does not depend on M_* and so will remain constant. Thus, r_B/r_J will be a slowly increasing function of time and eventually the presumption that $r_B \ll r_J$ fails.

3.3. Interface between molecular cloud region and the ISM

Although gas density and temperature in reality change gradually on entering the cloud from the ISM, for simplicity we assume here that these changes occur in a narrow layer. Integration of Eq.4 across this layer while taking into account mass conservation gives continuity of $\rho_g u_g^2 + P_g$ across the layer and integration of the mass conservation equation gives

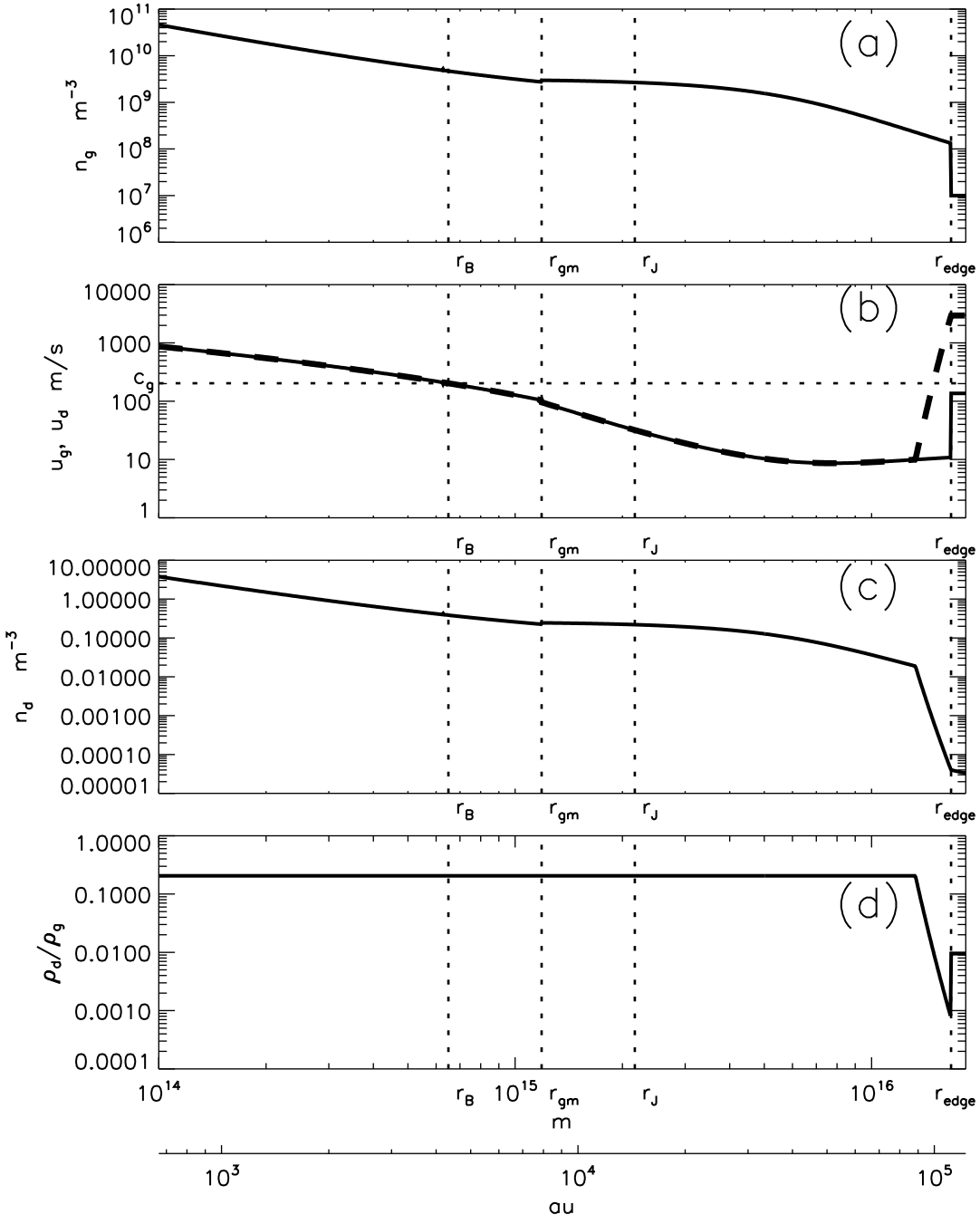

Fig. 1.— Model predictions assuming $\varepsilon_{BJ} = 0.3$, $M_* = 0.4 M_\odot$, $T_g = 10$ K, $T_g^{ISM} = 100$ K, and $n_g^{ISM} = 10^7 \mathrm{m}^{-3}$. (a) gas density, (b) solid line gives gas velocity, dashed line gives dust velocity, (c) dust density, (d) dust-to-gas mass ratio.

continuity of $\rho_g u_g$ across the layer. This yields Rankine-Hugoniot equations of the form

$$\bar{n}_g(r_{edge})\ \left(1+(\bar{u}_g(r_{edge}))^2\right) = \ \bar{n}_g^{ISM}\left(\ T_g^{ISM}/T_g + \ \left(\bar{u}_g^{ISM}\right)^2\right) \tag{41}$$

$$\bar{n}_g(r_{edge})\bar{u}_g(r_{edge}) = \bar{n}_g^{ISM}\ \bar{u}_g^{ISM} \tag{42}$$

where $\bar{n}_g^{ISM}, T_{ISM}$, and T_g are specified and $\bar{u}_g^{ISM}, r_{edge}$, $\bar{u}_g(r_{edge})$, and $\bar{n}_g(r_{edge})$ are to be determined. The bar indicates that densities are normalized to n_{gm} and velocities are normalized to $c_g = \sqrt{\kappa T_g/m_g}$. Using Eq.42 to substitute for $\bar{n}_g(r_{edge})\bar{u}_g(r_{edge})$ in Eq.41 gives

$$\bar{n}_g(r_{edge}) + \left(\frac{1}{\bar{n}_g(r_{edge})} - \frac{1}{\bar{n}_g^{ISM}}\right)\left(\bar{n}_g^{ISM}\ \bar{u}_g^{ISM}\right)^2 = \quad \bar{n}_g^{ISM}\ \frac{T_g^{ISM}}{T_g}. \tag{43}$$

However using Eq.10 evaluated in the ISM at r_{edge}, Eq.39 and Eq.33 give

$$\bar{n}_g^{ISM}\bar{u}_g^{ISM} = \ -\eta\varepsilon_{BJ}^2\ \frac{r_J^2}{r_{edge}^2} \tag{44}$$

while Eq.35 gives

$$\bar{n}_g(r_{edge}) \simeq \frac{2r_J^2}{r_{edge}^2} \tag{45}$$

so eliminating r_J^2/r_{edge}^2 between these equations gives

$$\bar{n}_g^{ISM}\bar{u}_g^{ISM} \simeq -\frac{\eta\varepsilon_{BJ}^2}{2}\bar{n}_g(r_{edge}). \tag{46}$$

Substituting for $\bar{n}_g^{ISM}\bar{u}_g^{ISM}$ in Eq.43 gives

$$-\frac{\left(\bar{n}_g(r_{edge})\right)^2}{\bar{n}_g^{ISM}}\left(\frac{\eta\varepsilon_{BJ}^2}{2}\right)^2 + \bar{n}_g(r_{edge})\left(1+\ \left(\frac{\eta\varepsilon_{BJ}^2}{2}\right)^2\right) - \quad \bar{n}_g^{ISM}\ \frac{T_g^{ISM}}{T_g} = 0, \tag{47}$$

a quadratic equation in $\bar{n}_g(r_{edge})$. Since ε_{BJ} is assumed small, an approximate solution to Eq.47 may be obtained by balancing the last two terms in which case

$$\bar{n}_g(r_{edge}) \simeq \frac{\bar{n}_g^{ISM}}{(1+\ \eta^2\varepsilon_{BJ}^4/4)}\ \frac{T_g^{ISM}}{T_g}\ . \tag{48}$$

Equation 45 then gives

$$\frac{2r_J^2}{r_{edge}^2} = \frac{\bar{n}_g^{ISM}}{(1+\ \eta^2\varepsilon_{BJ}^4/4)}\ \frac{T_g^{ISM}}{T_g} \tag{49}$$

so using Eq.33

$$r_{edge} \simeq c_g^2\sqrt{\frac{1+\ \varepsilon_{BJ}^4\eta^2/4}{2\pi G n_g^{ISM}\kappa T_g^{ISM}}}\ . \tag{50}$$

Equation 44 gives

$$u_g^{ISM} = -\eta\varepsilon_{BJ}^2 \frac{T_g^{ISM}}{2T_g} \frac{c_g}{(1+\varepsilon_{BJ}^4\eta^2/4)}, \tag{51}$$

which combined with Eq.42 and Eq.48 give

$$u_g(r_{edge}) = -\frac{\varepsilon_{BJ}^2\ \eta c_g}{2} \quad . \tag{52}$$

The gas mass between r_J and r_{edge} is

$$M_{r<r_{edge}} \simeq \int_{r_J}^{r_{edge}} \left(\rho_{gm} 2\frac{r_J^2}{r^2}\right) 4\pi r^2 dr \simeq 2c_g^4 \sqrt{\frac{1+\ \varepsilon_{BJ}^4\eta^2/4}{2\pi G^3 n_g^{ISM}\kappa T_g^{ISM}}}\ . \tag{53}$$

The mass inside the core region of radius r_J is using Eqs.35, 33 and 37

$$M_{r<r_J} \simeq \rho_{gm} \int_{r_{gm}}^{r_J} \frac{4\pi r^2}{1+r^2/6r_J^2} dr \simeq \rho_{gm} \frac{4\pi r_J^3}{3} \simeq \frac{M_*}{6\varepsilon_{BJ}}. \tag{54}$$

Table 3 shows quantities predicted by this analysis for $\varepsilon_{BJ} = 0.3$, $M_* = 0.4M_\odot$, $T_g = 10$ K, $T_g^{ISM} = 100$ K, molecular hydrogen, and $n_g^{ISM} = 10^7$ m^{-3}. Note that the gas flow velocities are subsonic (i.e. much smaller than the random or thermal velocity) both in the portion of the cloud external to r_B and in the ISM since in the portion of the cloud external to r_B gas flow velocities u_g are much slower than $c_g = \sqrt{\kappa T_g/m_g} = 200$ m/s and in the ISM the gas flow velocity u_g^{ISM} is much slower than $c_g^{ISM} = \sqrt{\kappa T_g^{ISM}/m_g} = 640$ m/s.

4. Dust

4.1. Overview of dust

The mass density of dust in the ISM is well established to be 1% of the gas mass density (Lilley 1955; Zubko *et al.* 2004). As mentioned earlier, it is commonly assumed that this 1% ratio also holds in a dense molecular cloud. However, Padoan *et al.* (2006) have recently cast doubt on such an assumption arguing that if the dust-to-gas mass ratio were indeed 1% in a dense molecular cloud, then the dust and column densities should have the same spectral power law, i.e., the spatial Fourier power spectra $S(k)$ of dust and gas images should be characterized by the same power law $S(k) \sim k^{-p}$. In fact, Padoan *et al.* (2006) found that p for the dust differs from p for the gas, indicating a lack of local proportionality between dust and gas.

	value	units	value	units	Reference
r_B	6.5×10^{14}	m	4.3×10^3	au	Eq.12
r_{gm}	1.2×10^{15}	m	7.9×10^3	au	Eq.2
r_J	2.2×10^{15}	m	1.4×10^4	au	Eq.33
n_{gm}	3.1×10^9	m^{-3}	3.1×10^3	cm^{-3}	Eq.37
$u_g(r_{gm})$	-91	m/s			Eq.40
c_g	2.0×10^2	m/s			Eq.9
$\dot{M}_g$	1.7×10^{16}	kg /s	2.7×10^{-7}	$M_\odot$ yr^{-1}	Eq.39
r_{edge}	1.7×10^{16}	m	1.1×10^5	au	Eq.50
r_{edge}/r_{Jeans}	7.7				
$u_g(r_{edge})$	-14	m/s			Eq.52
u_g^{ISM}	-1.4×10^2	m/s			Eq.51
c_g^{ISM}	6.4×10^2	m/s			Eq.9
$M_{r<r_{edge}}$	2.1×10^{31}	kg	10	$M_\odot$	Eq.53
$M_{r<r_J}$	4.4×10^{29}	kg	0.2	$M_\odot$	Eq.54
$M_{r<r_B}$	1.8×10^{28}	kg	0.01	$M_\odot$	Eq.29

Table 3: Calculated quantities for ϵ_{BJ} =0.3, $M_* = 0.4 M_\odot$, T_g=10 K, $c_g = 2 \times 10^2$ m/s

Takeuchi *et al.* (2005) have also pointed out that the dust/gas mass ratio in a cloud need not be the same as in the ISM because gas and dust might be subject to different processes. Goldsmith *et al.* (1997) showed in their Fig.22 that the observed dust-to-gas ratio varies by an order of magnitude as a function of position in a system of molecular clouds, i.e., the observed dust-to-gas mass ratio in a molecular cloud system is not, as in the ISM, fixed at 1%. As mentioned earlier, Fukue (2001) presented numerical calculations specifically demonstrating that accretion can enrich the dust-to-gas ratio. As also mentioned earlier, Fukue (2001) assumed that a Bondi accretion region was directly bounded by the ISM, i.e., did not take into account the molecular cloud scale where gas self-gravity is important. This omission resulted in calculated mass accretion rates lower than typical observed values (e.g., Fukue's nominal accretion rate was $\dot{M}_g \sim 10^{-10}\ M_\odot\ \mathrm{yr}^{-1}$ compared to the observed nominal $\dot{M}_g \sim 10^{-9}\ M_\odot$ to $10^{-7}\ M_\odot$ rates for pre-main sequence YSO's reported by Hartmann *et al.* (1998)). Since gas and dust density scale linearly with accretion rate, the low nominal accretion rate in Fukue's calculation corresponded to a very low dust density and hence optically thin dust. Higher accretion rates give higher dust densities and optically thick dust densities that correspond to the observed opacities of clouds. Nevertheless, Fukue's calculation had the interesting feature of predicting that in certain circumstances the accretion process could cause a thirty-fold increase in the dust-to-gas mass ratio.

We now argue that this enrichment reported by Fukue should be a basic property of dust/gas accretion systems, so the dust/gas mass density ratio in a cloud core should in general be substantially enriched relative to its 1% ISM ratio. Because the accretion region is now assumed to be bounded by a cloud core rather than by the ISM, this enrichment effect is demonstrated here in association with more realistic mass accretion rates.

Collision properties of gas and dust vary considerably in ISM, cloud, cloud core, and accretion regions. This variation is because the scale lengths are different and because the mean free paths are different. Dust is collisionally decoupled from gas in some regions, but strongly coupled in others. In particular, it turns out that dust is decoupled from gas in the ISM, strongly coupled in the molecular cloud and cloud core, but then can become decoupled again when dust-dust collisions result in dust coagulation. Dust-dust collisionality is closely related to dust opacity since the mean free path for dust-dust collisions is $l_{dd} = 1/n_d\sigma_d$ while the distance for unity optical depth is the same if light scattering is geometric, but larger by the factor $1/Q_{ext}$, where the efficiency factor Q_{ext} accounts for weaker than geometric scattering (i.e., Rayleigh) and for absorption.

Let us start with the ISM. Because of the low gas density in the ISM, dust is collisionally decoupled from gas so if the dust becomes charged, electromagnetic mechanisms can accelerate ISM dust grains to velocities much higher than the ~ 640 m/s ISM gas thermal velocity. Meyer *et al.* (1998), Yan & Lazarian (2003), Slavin *et al.* (2004), and Shukla & Stenflo (2005) have provided examples of such dust acceleration mechanisms.

In contrast, dust is collisionally coupled to gas in molecular clouds because of the high gas density. In cloud cores and/or accretion regions the dust density becomes so high that dust-dust collisions also become important. The condition for dust-dust collisions to be important corresponds approximately to the condition that the dust is optically thick. Thus, if there is an inner region where dust-dust collisions are important, regions external to this inner region will be shielded from central object optical emission and so will not experience any radiation pressure from the central object. Dust-dust collisions result in dust coagulation, a condition where the dust radius r_d increases while the overall dust mass density remains invariant. Coagulation has the dual effect of causing the dust to revert to being optically thin and collisionless. Collisionless, coagulated dust exposed to stellar radiation becomes charged via photo-emission and so must be described by dusty plasma dynamics rather than by gas dynamics. This dusty plasma regime will be considered in a future publication; preliminary results are presented in Bellan (2007).

4.2. Dust grain size assumption

Mathis, Rumpl, and Nordsieck (1977) reported observations showing that ISM dust grains have a size distribution scaling as $r_d^{-3.5}$ with a nominal lower limit radius $r_{low} = 0.005$ μm and a nominal upper limit $r_{high} = 0.25$ μm. This size distribution is commonly referred to as the MRN dust size distribution. Miyake & Nakagawa (1993) proposed that the dust size distribution in a circumstellar disk will have larger grains than given by the MRN distribution because in a circumstellar disk where the dust density is high, dust coagulates due to dust-dust collisions. More recently, Przygodda *et al.* (2003) and van Boekel *et al.* (2003) have reported direct observational evidence of grain growth in circumstellar disks while, in addition, Dullemond & Dominik (2005) provided detailed calculations showing a strong tendency for dust grain growth when dust grains collide with each other.

The $r_d^{-3.5}$ dust size distribution has important well-known statistical properties. Specifically, an $r_d^{-3.5}$ distribution implies (i) most of the mass is contained in the very small number of heavy grains and (ii) most of the surface area is contained in the very large number of light grains (Smith & Dwek 1998). Although the lightest dust grains provide most of the surface area, their radii are so much smaller than visible light wavelengths that their scattering is Rayleigh rather than geometric. Rayleigh scattering is weaker than geometric scattering by a factor r_d^4/λ^4 where λ is the wavelength of the radiation. Hence, despite being numerous, the very small radius grains are ineffectual at contributing to the optical depth at visible wavelengths so visible scattering will be due mainly to the larger grains which also contain most of the mass. Hence, for purposes of both mass inventory and optical depth we will consider that dust grains have a nominal radius $r_d = 0.1$ μm.

4.3. Dust velocity in the ISM

If the velocity of individual dust grains in the ISM were the result of thermal equilibration with gas molecules, the dust kinetic temperature would be the same as the gas molecule kinetic temperature in which case the random velocity of dust grains in the ISM would be $u_d^{ISM} \sim \sqrt{\kappa T_g/m_d} =$ 0.01 m/s. This velocity is so small that there would be insufficient dust flux entering a molecular cloud to populate the cloud with dust in a reasonable time. It has been proposed by several authors that dust attains a much larger random velocity in the ISM because dust is nearly collisionless in the ISM so that collective collisionless mechanisms such as shocks or turbulence could accelerate dust to very large velocities. As mentioned earlier, Meyer *et al.* (1998), Yan & Lazarian (2003), Slavin *et al.* (2004), and Shukla & Stenflo (2005) have presented collisionless mechanisms whereby dust grains are accelerated to velocities in the 10 km/s range.

A typical argument for collisionless acceleration is that a spatially and temporally random magnetic field develops with energy density in thermodynamic equipartition with the gas, i.e., $B^2/2\mu_0 \sim n_g^{ISM}\kappa T_g^{ISM}$ so

$$B \sim \sqrt{2\mu_0 n_g^{ISM}\kappa T_g^{ISM}} \sim 2\times 10^{-10} \quad \text{T}. \tag{55}$$

Gradients in this microgauss magnetic field then accelerate charged dust grains via electromagnetic forces so that the dust random kinetic energy becomes comparable to the magnetic energy density, i.e.,

$$\frac{1}{2}\rho_d^{ISM}\left(U_d^{ISM}\right)^2 \sim \frac{B^2}{2\mu_0} \tag{56}$$

where U_d^{ISM} is a random velocity that could be pointing in any direction. The nominal random velocity U_d^{ISM} attained by the accelerated grains is thus the dust Alfvén velocity given by $v_A^2 = B^2/\mu_0\rho_d^{ISM}$. Combining Eqs.55 and 56 gives the random velocity to be

$$U_d^{ISM} \simeq \sqrt{\frac{2\kappa T_g^{ISM}}{m_g}\frac{\rho_g^{ISM}}{\rho_d^{ISM}}}, \tag{57}$$

a relationship dependent on the dust-to-gas mass density ratio. Equation 57 gives $U_d^{ISM} \sim$ 9.3 km/s for a nominal 1% ISM dust-to-gas mass ratio and $T_g^{ISM} = 100$ K. This velocity is six orders of magnitude larger than the velocity predicted by thermal equilibration of individual dust grains with gas molecules. Because the dust is assumed to be accelerated by collisionless processes, it will not in general have a Maxwellian distribution, and in fact it would be reasonable to expect that each dust grain has a velocity $\sim U_d^{ISM}$ but with a random direction. This situation would be similar to the neutrons emitted from a fission reaction since such neutrons all have the same kinetic energy but have random velocity directions.

The mean radial velocity of dust grains entering a spherical molecular cloud can be determined by considering the radial velocity component of these dust grains at the surface of the sphere. If $\hat{s}$ denotes the inwards normal to the surface at some point on the surface of the sphere, then the radial velocity of a dust grain entering the sphere at this point is $U_d^{ISM}\cos\theta$ where θ is the angle between the dust grain vector velocity and $\hat{s}$. The angle θ must lie between $-\pi/2$ and $\pi/2$ since dust grains having θ outside this range will not enter the sphere. Other than being restricted to the range $-\pi/2 < \theta < \pi/2$, the angle θ is random. The dust grains have equal probability of having any angle θ between 0 and 2π so the probability of a dust grain angle being between θ and $\theta + d\theta$ is $d\theta/2\pi$. The mean radial velocity of dust grains entering a molecular cloud from the ISM is thus

$$u_d^{ISM} = \int_{-\pi/2}^{\pi/2} U_d^{ISM}\cos\theta\,\frac{d\theta}{2\pi} = \frac{1}{\pi}U_d^{ISM} \simeq 3 \text{ km/s}. \tag{58}$$

The question of whether dust exits a molecular cloud will be addressed in the next section.

4.4. Dust entrainment by gas in molecular cloud

The dust equation of motion can be expressed as

$$u_d \frac{du_d}{dr} = -\frac{G}{r^2}\left(M_* + \int_{r_*}^{r} 4\pi\xi^2 \left(\rho_g(\xi) + \rho_d(\xi)\right) d\xi\right) - (u_d - u_g)\frac{\rho_g}{m_d}\sigma_d\sqrt{c_g^2 + (u_d - u_g)^2} \tag{59}$$

where it is recalled that both u_d and u_g are negative corresponding to radial inward motion.

We wish to investigate the possibility that ρ_d/ρ_g could increase from its 1% ISM value as dust and gas enter the cloud, core, and Bondi accretion region. However, we will assume that ρ_d/ρ_g remains sufficiently small compared to unity that the back-reaction of dust on gas dynamics can be ignored. Thus, $u_g(r)$ and $\rho_g(r)$ are assumed to remain as discussed in Sec.3.1 and 3.2. Dust enters the cloud from the ISM with a velocity much higher than the gas thermal and fluid velocities but then collides with the gas, thereby slowing down until moving at nearly the same inward fluid velocity as the gas. Collisions thus cause the dust to become entrained by the gas inflow (Fukue 2001).

The collisional slowing down can be estimated by assuming that the gravitational force term in Eq.59 can be ignored because of the high dust velocity. Furthermore, u_d is much larger than both u_g and c_g when the dust enters the cloud from the ISM. In this case and using

$$\frac{\sigma_d}{m_d} = \frac{3}{4 r_d \rho_d^{int}} \tag{60}$$

where $\rho_d^{int} \simeq 2 \times 10^3$ kg m^{-3} is the intrinsic mass density of the dust, Eq.59 becomes

$$\frac{du_d}{dr} = -\, u_d \, \frac{3\rho_g(r)}{4 r_d \rho_d^{int}}. \tag{61}$$

Integration of Eq. 61 starting from the cloud edge and going inwards gives

$$u_d(r) = u_d(r_{edge}) \exp\left(-\int_r^{r_{edge}} \frac{3\rho_g(\xi)}{4 r_d \rho_d^{int}} d\xi\right). \tag{62}$$

The dashed line in Fig. 1(b) shows the dust velocity given by Eq.62 for the gas density given in Fig. 1(a) and assuming a 3 km/s dust mean radial entrance velocity. It is seen that the dust rapidly slows down until it achieves the same velocity as the gas at which point it is assumed to be entrained by the gas. Dust will thus become entrained by gas at a radius $r_{entrain}$ where $r_{entrain}$ satisfies

$$u_d^{ISM} \exp\left(-\int_{r_{entrain}}^{r_{edge}} \frac{3\rho_g(r)}{4 r_d \rho_d^{int}} dr\right) \sim u_g^{edge} \sim c_g/20. \tag{63}$$

Using Eq.58 to estimate u_d^{ISM}, Eq.63 becomes

$$\int_{r_{entrain}}^{r_{edge}} \frac{3\rho_g(r)}{4r_d\rho_d^{int}}dr \sim \ln\left(\frac{20u_d^{ISM}}{c_g}\right) \simeq 5.7 \quad . \tag{64}$$

If the gas density in the $r >> r_J$ portion of the cloud is sufficiently large to provide entrainment, then $\rho_g(r)$ can be approximated in this region as $\rho_g(r) \simeq 2\rho_{gm}r_J^2/r^2$ so Eq.64 becomes

$$\frac{3\rho_{gm}r_J}{2r_d\rho_d^{int}}\left(\frac{r_J}{r_{entrain}} - \frac{r_J}{r_{edge}}\right) \simeq 5.7 \tag{65}$$

Table 3 gives $r_{edge}/r_J \simeq 7.7$ and since $3\rho_{gm}r_J/2\rho_d^{int}r_d = 1.7 \times 10^2$ this gives $r_{entrain} \simeq 6r_J$. As assumed, the dust becomes entrained by the gas at a location in the $r >> r_J$ portion of the cloud.

The entrainment of dust by gas means that the radial flow of dust from the ISM to the cloud is one-way inwards, i.e., there is no radial outward flow of individual dust grains from the cloud back to the ISM. This one-way inward behavior of dust grains is in contrast to gas. Because gas molecules collide with each other, some gas molecules have inwards radial velocities and some have outwards radial velocities. However, there are more inwards than outwards moving gas molecules and the net inwards gas fluid velocity at r_{edge} is a consequence of this difference. The situation is somewhat analogous to a home vacuum cleaner ingesting macroscopic particles and air; individual air molecules in the vacuum hose have inwards or outwards velocities with magnitude of the order of the air thermal velocity, the mean air velocity in the hose is inwards and much slower than the air thermal velocity, and all the macroscopic particles in the hose have inwards velocities.

4.5. Enrichment of dust-to-gas mass ratio

Equations 10 and 11 can be evaluated at any radius. Evaluating at r_{edge} and at r_{gm} gives

$$4\pi r_{edge}^2\rho_g^{ISM}u_g^{ISM} = 4\pi r_{gm}^2\rho_g(r_{gm})u_g(r_{gm}) \tag{66}$$

$$4\pi r_{edge}^2\rho_d^{ISM}u_d^{ISM} = 4\pi r_{gm}^2\rho_d(r_{gm})u_d(r_{gm}). \tag{67}$$

Dividing Eq.66 by Eq.67 gives

$$\frac{\rho_d(r_{gm})/\rho_g(r_{gm})}{\rho_d^{ISM}/\rho_g^{ISM}} = \frac{u_d^{ISM}/u_g^{ISM}}{u_d(r_{gm})/u_g(r_{gm})} \quad . \tag{68}$$

Since the dust is certainly fully entrained by the time it reaches r_{gm} we may assume $u_d(r_{gm})/u_g(r_{gm}) = 1$. Using Eq.51 to give u_g^{ISM} and Eqs. 57 and 58 to give u_d^{ISM}, Eq.68

becomes

$$\frac{\rho_d(r_{gm})}{\rho_g(r_{gm})} = \frac{2+\varepsilon_{BJ}^4\eta^2/2}{\pi\eta\varepsilon_{BJ}^2}\sqrt{\frac{2T_g}{T_g^{ISM}}\frac{\rho_d^{ISM}}{\rho_g^{ISM}}}. \tag{69}$$

Fig. 1(c) shows the dust density and Fig.1(d) shows the dust-to-gas mass ratio as function of radius, showing that enrichment occurs so that the dust-to-gas ratio increases from its 0.01 ISM value to become somewhat less than unity. For the example parameters in Table 3 and a 1% ISM dust-to-gas mass ratio, Eq.69 predicts $\rho_d(r_{gm})/\rho_g(r_{gm}) = 0.2$ for $\varepsilon_{BJ} = 0.3$, $T_g = 10$ K, and $T^{ISM} = 100$ K; this corresponds to the saturated value in Fig.1(d) and represents a twenty-fold enrichment of the dust-to-gas mass ratio over its ISM value.

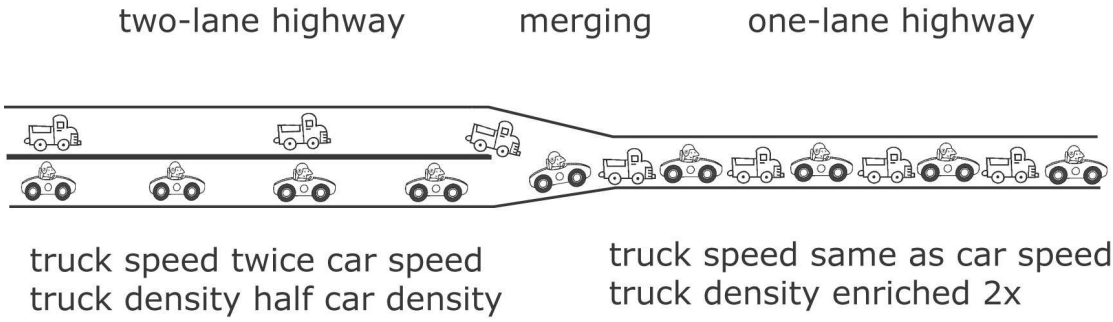

Fig. 2.— Because trucks entering the one-lane segment slow down whereas cars do not, the truck-to-car density ratio is enriched in the one-lane segment compared to the density ratio in the two-lane segment.

An everyday example of the enrichment effect predicted by Eq.68 is where traffic on a two-lane highway merges to flow on a one-line highway as sketched in Fig.2. In the two-lane segment (left of figure), the trucks move at twice the speed of the cars and have half the density of the cars. The cars are assumed to have the same speed in the two-lane and one-lane highway segments, i.e., the cars do not slow down. The trucks have to slow down when they enter the one-lane segment because in the one-lane segment the trucks must go at the same speed as the cars. Slowing down by a factor of two causes the number of trucks per length of road to double because in steady-state the flux of trucks (product of the truck speed and the trucks per length of road) must be the same in the one- and two-lane segments. The density of trucks to cars is thus enriched by a factor of two in the one-lane highway segment compared to its value in the two-lane highway segment.

4.6. Radiation pressure and optical depth

Abbas *et al.* (2003) used a calibrated electrodynamic balance to measure the radiation pressure force exerted on a r_d =0.125 μm particle by a 0.532 nm wavelength laser. They found that the force exerted by a laser intensity 8×10^5 W m^{-2} was 3×10^{-17} N. If such a particle were in the gravitational field of a star with luminosity L_*, the radiation pressure force on the particle would thus be

$$F_{rad} = \frac{L_* e^{-\tau(r)}}{4\pi r^2} \frac{3 \times 10^{-17}}{8 \times 10^5} \quad \mathrm{N} \tag{70}$$

where

$$\tau(r) = \int_{r_*}^{r} Q_{ext} n_d(\xi) \sigma_d d\xi \tag{71}$$

is the optical depth for light traveling from the star to radius r and Q_{ext} is the extinction efficiency. The gravitational force would be

$$F_g = \frac{m_g M_* G}{r^2} \quad \mathrm{N} \tag{72}$$

so the ratio would be

$$\frac{F_{rad}}{F_g} = \frac{L_* e^{-\tau(r)}}{4\pi} \frac{3 \times 10^{-17}}{8 \times 10^5} \frac{1}{m_g M_* G}. \tag{73}$$

Assuming $m_g = 10^{-17}$ kg for a nominal $r_d = 10^{-7}$ m dust grain gives

$$\frac{F_{rad}}{F_g} = \ 0.9 e^{-\tau(r)} \frac{L_*/L_\odot}{M_*/M_\odot} \tag{74}$$

so a dust grain could in principle be subject to significant radiation force if $\tau \ll 1$ as was proposed by Fukue. Table 1 of Abbas *et al.* (2003) gives the calculated radiation pressure efficiency $Q_{pr} = 0.28$ for a $r_d = 0.125$ μm dust grain illuminated by 532 nm light. This is in reasonable agreement with their measured value $Q_{pr} = 0.22$; Abbas *et al.* (2003) also presented a calculated extinction efficiency $Q_{ext} = 0.33$ and a calculated scattering efficiency $Q_{sca} = 0.16$ that together would be in reasonable agreement with the measured Q_{pr}. Figure 1(c) shows that dust for the representative parameters discussed here has a density $n_d \simeq 1$ m^{-3} at r_B and that this density increases for $r < r_B$. Table 3 gives $r_B = 6.5 \times 10^{14}$ m. Thus, a lower bound for the optical depth at r_B can be estimated using

$$\tau(r_B) > \ Q_{ext} n_d(r_B) \sigma_d r_B = 0.33 \times 1 \times \pi \times (10^{-7})^2 \times 6.5 \times 10^{14} = 6.7 \quad . \tag{75}$$

Star light would thus be attenuated by a factor greater than $\exp(-6.7) \simeq 10^{-3}$ and so optical radiation from the star should be fully extinguished by the time it reaches r_B in which case

there would be no significant radiation pressure on dust at radii of the order of r_B or larger. The reasons why we differ from Fukue by concluding that radiation pressure is unimportant are (i) Fukue's adiabatic assumption resulted in gas that was 1600 times hotter at small r so for a given pressure the gas density would be 1600 times less and so for a given dust-to-gas ratio, the dust density would be much lower, (ii) Fukue also used a much lower value of Q_{ext} than the value given in Abbas *et al.* (2003).

5. Discussion

The logical requirement that the Bondi length must be smaller than the Jeans length introduces the dimensionless parameter ε_{BJ} given by the ratio of these lengths. An intermediate distance r_{gm} can be defined as the geometric mean of the Bondi and Jeans lengths so, if the two lengths are well separated, r_{gm} is much larger than the Bondi length but much smaller than the Jeans length. Thus, r_{gm} constitutes the large r limit of the solution to the Bondi problem and the small r limit of the solution to the Jeans problem. Matching the Bondi and Jeans solutions at r_{gm} provides a solution valid over scales ranging from smaller than the Bondi length to larger than the Jeans length. This allows accounting for transonic flow, mass accretion, and gravitational self-confinement in one self-consistent solution to the gas equation.

By assuming that the dust mass density and energy density are not larger than the corresponding gas densities, the gas equations can be evaluated ignoring interaction with dust. Once the gas behavior has been worked out, the dust can be considered as moving through a pre-determined gas profile that retards the dust due to frictional drag. The dust slows down greatly whereas the gas velocity changes relatively little, a distinction that enriches the dust-to-gas mass ratio. Plausible values of ε_{BJ} suggest that the dust-to-gas mass ratio will always be enriched to be somewhat less than unity, because at unity the assumption that the gas is unaffected by dust fails. The high dust density at small radius means that dust-dust collisions will become important and cause coagulation of dust. This coagulation will cause the dust to become optically thin and collisionless again. Because the coagulated dust is optically thin, it will absorb photons from the star and become electrically charged due to photo-emission of electrons. Two-dimensional motion of collisionless, charged dust in a gravitational field resulting in a poloidal field dynamo has been discussed in Bellan (2007); three dimensional motion and resulting poloidal/toroidal field dynamo action will be discussed in a future publication.

The author wishes to thank an anonymous referee for his/her thoughtful comments.

REFERENCES

Abbas, M. M., Craven, P. D., Spann, J. F., Witherow, W. K., West, E. A., Gallagher, D. L., Adrian, M. L., Fishman, G. J., Tankosic, D., LeClair, A., Sheldon, R., & Thomas, E. 2003. Radiation pressure measurements on micron-size individual dust grains. *Journal of Geophysical Research-Space Physics*, **108**(A6). 1229.

Bellan, P. M. 2007. Consideration of the relationship between Kepler and cyclotron dynamics leading to prediction of a nonmagnetohydrodynamic gravity-driven Hamiltonian dynamo. *Physics of Plasmas*, **14**. Art. No. 122901.

Bellan, P. M., You, S., & Hsu, S. C. 2005. Simulating astrophysical jets in laboratory experiments. *Astrophysics and Space Science*, **298**(1-2), 203–209.

Bondi, H. 1952. On Spherically Symmetrical Accretion. *Monthly Notices of the Royal Astronomical Society*, **112**(2), 195–204.

Bonnor, W. B. 1956. Boyles Law and Gravitational Instability. *Monthly Notices of the Royal Astronomical Society*, **116**(3), 351–359.

Dullemond, C. P., & Dominik, C. 2005. Dust coagulation in protoplanetary disks: A rapid depletion of small grains. *Astronomy and Astrophysics*, **434**(3), 971–986.

Ebert, R. 1955. ber die Verdichtung von H I-Gebieten. *Z. Astrophysik*, **37**, 217.

Evans, N. J., Rawlings, J. M. C., Shirley, Y. L., & Mundy, L. G. 2001. Tracing the mass during low-mass star formation. II. Modeling the submillimeter emission from preprotostellar cores. *Astrophysical Journal*, **557**(1), 193–208. Part 1.

Fukue, J. 2001. Dust-gas accretion onto a luminous object. *Publications of the Astronomical Society of Japan*, **53**(2), 275–283.

Goldsmith, P. F., Bergin, E. A., & Lis, D. C. 1997. Carbon monoxide and dust column densities: The dust-to-gas ratio and structure of three giant molecular cloud cores. *Astrophysical Journal*, **491**(2), 615–637. Part 1.

Hartmann, L., Calvet, N., Gullbring, E., & D'Alessio, P. 1998. Accretion and the evolution of T Tauri disks. *Astrophysical Journal*, **495**(1), 385–400. Part 1.

Hsu, S. C., & Bellan, P. M. 2002. A laboratory plasma experiment for studying magnetic dynamics of accretion discs and jets. *Monthly Notices of the Royal Astronomical Society*, **334**(2), 257–261.

Lamers, H. J. G. L. M., & Cassinelli, J. P. 1999. *Introduction to Stellar Winds*. Cambridge: Cambridge University Press. p.166.

Lilley, A. E. 1955. Association of Gas and Dust from 21-Cm Hydrogen Radio Observations. *Astrophysical Journal*, **121**(3), 559–568.

Meyer, J. P., Drury, L. O., & Ellison, D. C. 1998. A cosmic-ray composition controlled by volatility and A/Q ratio. SNR shock acceleration of gas and dust. *Space Science Reviews*, **86**(1-4), 179–201.

Miyake, K., & Nakagawa, Y. 1993. Effects of Particle-Size Distribution on Opacity Curves of Protoplanetary Disks around T-Tauri Stars. *Icarus*, **106**(1), 20–41.

Padoan, P., Cambresy, L., Juvela, M., Kritsuk, A., Langer, W. D., & Norman, M. L. 2006. Can we trust the dust? Evidence of dust segregation in molecular clouds. *Astrophysical Journal*, **649**(2), 807–815. Part 1.

Przygodda, F., van Boekel, R., Abraham, P., Melnikov, S. Y., Waters, L. B. F. M., & Leinert, C. 2003. Evidence for grain growth in T Tauri disks. *Astronomy and Astrophysics*, **412**(2), L43–L46.

Shukla, P. K., & Stenflo, L. 2005. The cross-field acceleration of charged dust grains by the ponderomotive force of compressional waves in dusty plasmas. *Astrophysical Journal*, **629**(2), L93–L95. Part 2.

Slavin, J. D., Jones, A. P., & Tielens, A. G. G. M. 2004. Shock processing of large grains in the interstellar medium. *Astrophysical Journal*, **614**(2), 796–806. Part 1.

Smith, R. K., & Dwek, E. 1998. Soft X-ray scattering and halos from dust. *Astrophysical Journal*, **503**(1), 831–842.

Takeuchi, T., Clarke, C. J., & Lin, D. N. C. 2005. The differential lifetimes of protostellar gas and dust disks. *Astrophysical Journal*, **627**(1), 286–292. Part 1.

van Boekel, R., Waters, L. B. F. M., Dominik, C., Bouwman, J., de Koter, A., Dullemond, C. P., & Paresce, F. 2003. Grain growth in the inner regions of Herbig Ae/Be star disks. *Astronomy and Astrophysics*, **400**(3), L21–L24.

Yan, H., & Lazarian, A. 2003. Grain acceleration by magnetohydrodynamic turbulence: gyroresonance mechanism. *Astrophysical Journal*, **592**, L33–L36.

Zubko, V., Dwek, E., & Arendt, R. G. 2004. Interstellar dust models consistent with extinction, emission, and abundance constraints. *Astrophysical Journal Supplement Series*, **152**(2), 211–249.